The influence of the conduction band of $BaCl_2$ on the thermal quenching of the Tm^{2+} $4f^{12}5d^1 \rightarrow 4f^{13}$ and $4f^{13} \rightarrow 4f^{13}$ luminescence in orthorhombic $BaCl_2$:$Tm^{2+/3+}$

Plokker, M. P.; Hintzen, H. T.

DOI
10.1016/j.omx.2024.100389

Publication date
2025

Document Version
Final published version

Published in
Optical Materials: X

Optical Materials: X 25 (2025) 100389

Contents lists available at ScienceDirect

Optical Materials: X

journal homepage: www.journals.elsevier.com/optical-materials-x

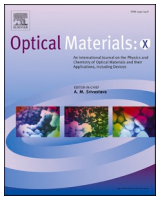

The influence of the conduction band of $BaCl_2$ on the thermal quenching of the Tm^{2+} $4f^{12}5d^1 \rightarrow 4f^{13}$ and $4f^{13} \rightarrow 4f^{13}$ luminescence in orthorhombic $BaCl_2$:$Tm^{2+/3+}$

M.P. Plokker *, H.T. Hintzen

Delft University of Technology, Faculty of Applied Sciences, Dept. Radiation Science and Technology, Mekelweg 15, 2629, JB Delft, the Netherlands

A B S T R A C T

The positioning of the Tm^{2+} $4f^{12}5d^1$ and $4f^{13}$ energy levels as relative to the conduction band of the orthorhombic $BaCl_2$ host lattice has been determined. Therefore, the energies of the Tm^{2+} $4f^{12}5d^1$-and excited $4f^{13}$-level were retrieved, as relative to the Tm^{2+} $4f^{13}$ ground state. In addition, the energy for exciton creation in the orthorhombic $BaCl_2$ host lattice was established, from which the bandgap energy was determined. This value was found to correspond quite well to known literature values. Furthermore, the Tm^{3+}-Cl^- charge transfer transition was determined, from which the energy difference between the Tm^{2+} $4f^{13}$ ground state and the top of the $BaCl_2$ valence band was deduced. A host referred binding energy scheme deduced for $BaCl_2$:Tm^{2+} then showed that the lowest energy Tm^{2+} $4f^{12}5d^1$-levels are positioned 0.3–0.5 eV below the $BaCl_2$ conduction band. Room temperature photo-excitation into this level will then most likely result in thermal ionization effects that have an impact on the Tm^{2+} $4f^{12}5d^1 \rightarrow 4f^{13}$ and $4f^{13} \rightarrow 4f^{13}$ luminescence and corresponding quantum yield.

1. Introduction

Over the years, various Tm^{2+}-doped halides have been studied for different applications. These include: AF_2:Tm^{2+} (A = Ca, Ba, Sr) compounds for maser applications [1–5]; $CsCaX_3$:Tm^{2+} (X = Cl, Br, I), $RbCaI_3$:Tm^{2+} and ACl_2:Tm^{2+} (A = Ca, Sr, Ba) materials for upconversion utilizations [6–13]; and more recently NaX:Tm^{2+}, CaX_2:Tm^{2+}, $CsCaX_3$:Tm^{2+} (X = Cl, Br, I) and SrI_2:Tm^{2+} materials for use in luminescent solar concentrators [5,14–18]. Also investigated, for their peculiar spectroscopic properties, were $AZnCl_4$:Tm^{2+} complexes (A = Sr, Ba) [19].

In case of Tm^{2+} doped in orthorhombic $BaCl_2$, the quenching dynamics was previously investigated by Grimm et al [12]. However, this study raised several questions. We have therefore conducted a follow-up study [20] to provide a clarification on the nature and quenching mechanisms of the Tm^{2+} $4f^{12}5d^1 \rightarrow 4f^{13}$ emissions. It was argued that the thermal quenching of the Tm^{2+} $4f^{12}5d^1 \rightarrow 4f^{13}$ luminescence is due to interband crossing of the Tm^{2+} $(^3H_6,5\ d^1)_{S\ =\ 1/2}$ and $(^3H_6,5\ d^1)_{S\ =\ 3/2}$, lowest energy $4f^{12}5d^1$ levels, with the Tm^{2+} $^2F_{7/2}$ ground state in the configurational coordinate diagram [21,22]. In addition, it has to be expected that the lowest energy Tm^{2+} $4f^{12}5d^1$-levels are positioned close to the conduction band of the $BaCl_2$ host lattice [20].

Therefore, in this current work, we will report the role of the $BaCl_2$ conduction band on the thermal quenching of the Tm^{2+} $4f^{12}5d^1 \rightarrow 4f^{13}$ luminescence. For that purpose a host-referred binding energy scheme was constructed from our measurements in combination with literature data.

2. Experimental methods

2.1. Sample Synthesis

For this study, the $BaCl_2$:$Tm^{2+/3+}$ powder sample from our recent work [20] was adopted. An additional $BaCl_2$:Tm^{3+} powder sample was prepared by mixing $BaCl_2$ (Sigma-Aldrich 99.9 %) with 1.5 mol % $TmCl_3$ (Sigma-Aldrich 99.9 %). This mixture was ground into a homogenous powder in an achate mortar, subsequently transferred into a quartz ampoule and attached to a vacuum/inert gas system. The system was then evacuated to 10^{-1} mbar and purged three times with dry nitrogen. The ampoule was subsequently evacuated to 10^{-3} mbar, after which the homogeneous powder was heated for 2.5 min using four Tecla burners. After liquification of the powder mixture, the heating was stopped and the sample was cooled down to room temperature. The now solidified sample was then removed from the ampoule and ground into a fine powder. All handlings were performed under inert and dry conditions in a nitrogen filled glovebox (MBraun, Garching, Germany).

Note that we will study the $BaCl_2$:$Tm^{2+/3+}$ sample to obtain the relative energy between the Tm^{2+} $4f^{12}5d^1$-and $4f^{13}$-levels, whereas for the $BaCl_2$:Tm^{3+} sample we will investigate the position of the Tm^{3+}-Cl^-

* Corresponding author.
E-mail address: maartenplokker@hotmail.com (M.P. Plokker).

https://doi.org/10.1016/j.omx.2024.100389
Received 24 August 2024; Received in revised form 27 October 2024; Accepted 1 December 2024
Available online 8 December 2024

Charge Transfer (CT) band. In addition, the $BaCl_2$ host bandgap energy will be examined for both samples and comparted to literature.

2.2. Characterisation

The X-Ray Diffraction (XRD) patterns of the powder samples were acquired with a Philips X'pert-Pro diffractometer (Philips, Eindhoven, The Netherlands) in Bragg-Bretano geometry using CuK_α radiation. The measurements took place at room temperature from 10° to 80° 2-theta with a 0.008° resolution. In addition, the Tm concentration in the samples was determined via Inductively Coupled Plasma–Optical Emission Spectroscopy (ICP-OES) measurements using a Perkin Elmer Optima 4300DV spectrometer (Perkin Elmer, Waltham Massachusetts, USA). Diluted standards of Tm and Ba with known concentrations were used to constitute an intensity-concentration calibration line. Furthermore, diffuse reflectance spectra were obtained with a Bruker Vertex V80 spectrometer (Bruker, Karlsruhe, Germany). The determined Tm^{2+} $4f^{13}\rightarrow4f^{13}$ and Tm^{3+} $4f^{12}\rightarrow4f^{12}$ Kubelka-Munk absorptions were used to estimate the Tm^{2+}/Tm^{3+} ratio present in the samples.

2.3. Luminescence measurements

The low temperature UV-NIR excitation and emission spectra were obtained using a Xenon lamp coupled to a double monochromator with three gratings and a R7600U–20HV–800V PMT, H1033A-75 NIR-PMT or C9100-13 EM-CCD (all Hamamatsu Photonics, Hamamatsu, Japan) that was in turn attached to a single monochromator with three gratings. The emission spectra were corrected for the wavelength dependent sensitivity of the detectors, with help of a calibrated EPLAB NBS 1000W Quartz Iodine lamp. In addition, low temperature VUV-UV excitation measurements were performed in the wavelength range of 160–1300 nm, using a Hamamatsu L1835 water-cooled deuterium lamp and the aforementioned PMTs and CCD as coupled to the same monochromator configuration. For these measurements, the samplechamber and monochromators were flushed with dry nitrogen, and subsequently evacuated to 10^{-6} mbar. The captured VUV-UV excitation spectra were corrected for the spectrum of the deuterium lamp. This latter spectrum was obtained using Sodium Salicylate (NaSal) for which a constant quantum efficiency over the VUV-UV range down to 160 nm was taken [23,24].

Throughout this study, the samples were heated and cooled by an APD Cryogenic Helium cooler (APD Cryogenics, Allentown Pennsylvania, USA) combined with an Lakeshore temperature controller (Lakeshore Cryotronics, Westerville Ohio, USA). Special airtight sample holders were used for all measurements to prevent unwanted hygroscopic and oxidation reactions in ambient atmospheres [25].

3. Results and discussion

3.1. Sample Characterisation

As discussed by Brixner et al. [26], anhydrous $BaCl_2$ exhibits two temperature-dependent structural modifications. At high temperatures, the β-form with cubic rock-salt type structure and space group *Fm3m* (No. 225) is formed. While at low temperatures, the α-form with orthorhombic cotunnite $PbCl_2$ structure and space group *Pnma* (No. 62) emerges. Fig. 1 shows the XRD pattern of the $BaCl_2$:Tm^{3+} (blue) and $BaCl_2$:$Tm^{2+/3+}$ (red) samples. The patterns match with the green reference pattern of the α-form. The Ba^{2+} ions in the orthorhombic *Pnma* modification have C_S point group site symmetry, combined with a 9-fold anion coordination geometry. Upon substituting Tm^{2+} (est. 1.2 p.m.) on the Ba^{2+}-site (1.47 p.m.) [27], the long Tm^{2+}-Cl^- distances will result in a weak crystal field.

Fig. 2 shows the Kubelka-Munk (K-M) absorption spectra of the $BaCl_2$:Tm^{3+} (blue) and $BaCl_2$:$Tm^{2+/3+}$ (red) samples. In this figure, the Tm^{3+} absorption peaks are indicated in green, whereas the ones related to Tm^{2+} are portrayed in purple. Note that we will use the short hand notation $^{2S+1}L_J$ to assign the Tm^{3+} $4f^{12}$-and Tm^{2+} $4f^{13}$-levels, and $(^{2S+1}L_J,5\ d^1)S$ to refer to the excited Tm^{2+} $4f^{12}5d^1$-levels. In this latter notation, $^{2S+1}L_J$ represents the state of $4f^{12}$ and S denotes the total electron spin of the excited state.

The K-M spectrum of the $BaCl_2$:$Tm^{2+/3+}$ sample was analyzed before in our recent study [20], where the different Tm^{2+} and Tm^{3+} absorption peaks were classified in accordance to the Dieke diagram [28]. The sharp absorption peaks at around 700, 800 and 1230 nm were respectively linked to the Tm^{3+} $^3H_6\rightarrow{}^3F_{2,3}$, $^3H_6\rightarrow{}^3H_4$ and $^3H_6\rightarrow{}^3H_5$ line-absorptions due to $4f^{12}\rightarrow4f^{12}$ transitions. Furthermore, the weak absorption peak near 1140 nm was associated with.

the Tm^{2+} $^2F_{7/2}\rightarrow{}^2F_{5/2}$ $4f^{13}\rightarrow4f^{13}$ line-absorption and the broad absorption band near 600 nm could be attributed to the Tm^{2+} $^2F_{7/2}\rightarrow(^3H_6,5\ d^1)_{S\ =\ 1/2}$ transition, which represents a $4f^{13}\rightarrow4f^{12}5d^1$ absorption [12]. A comparison between the absorption patterns of the $BaCl_2$:$Tm^{2+/3+}$ and $BaCl_2$:Tm^{3+} samples, reveals that the latter only contains Tm^{3+}.

From the ICP-OES measurements, the total Tm (i.e. Tm^{2+} plus Tm^{3+}) concentrations in the $BaCl_2$:$Tm^{2+/3+}$ and $BaCl_2$:Tm^{3+} samples were

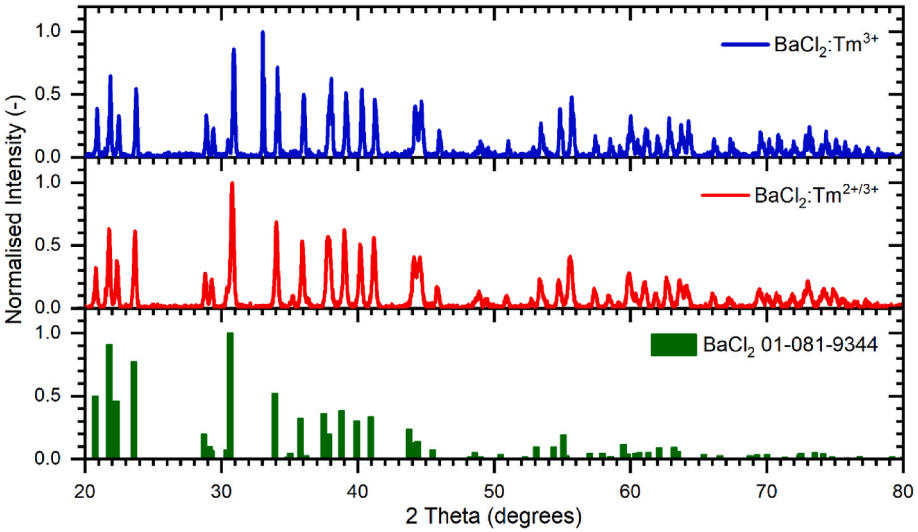

Fig. 1. Normalized powder X-ray diffraction patterns of the $BaCl_2$:Tm^{3+} (blue) and $BaCl_2$:$Tm^{2+/3+}$ (red) samples at room temperature. Both patterns match the reference pattern of orthorhombic $BaCl_2$ (green) with cotunnite $PbCl_2$ structure and space group *Pnma* (No. 62).

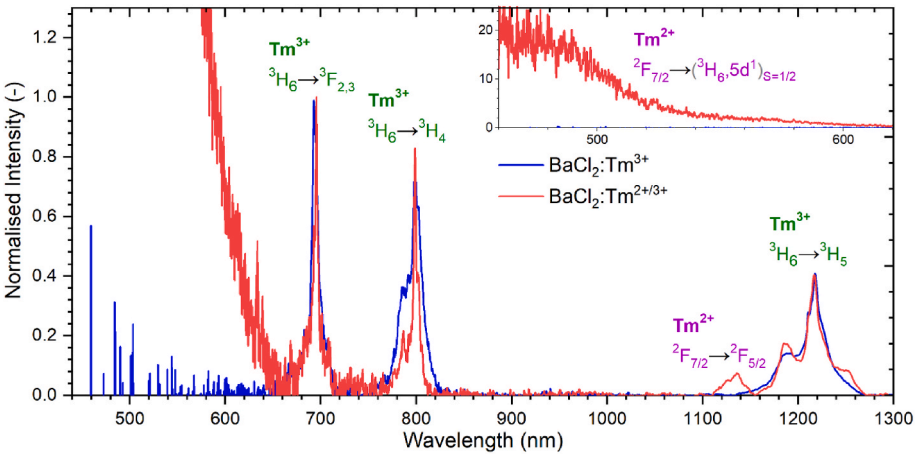

Fig. 2. The Kubelka-Munk (K–M) absorption spectra of the $BaCl_2$:Tm^{3+} (blue) and $BaCl_2$:$Tm^{2+/3+}$ (red) samples as normalized on the Tm^{3+} $^3H_6 \rightarrow {}^2F_{2,3}$ absorption. The related Tm^{3+} absorption peaks are labelled by their transition in green. For Tm^{2+}, the absorptions and related transitions are indicated in purple. The inset shows the intense Tm^{2+} $^2F_{7/2} \rightarrow (^3H_6, 5\ d^1)_{S\ =\ 1/2}$ absorption present in the $BaCl_2$:$Tm^{2+/3+}$ sample.

respectively determined at 1.1 ± 0.1 and 1.5 ± 0.1 mol %. As described in our previous work on NaI:Tm^{2+} [14] and our recent study on $BaCl_2$:$Tm^{2+/3+}$ [20], the diffuse reflectance measurements enable it to estimate the Tm^{2+}/Tm^{3+} ratios in our samples. This ratio was found to be 3/8 for the $BaCl_2$:$Tm^{2+/3+}$ sample and 0/1 for the $BaCl_2$:Tm^{3+} sample. Upon multiplying these ratio's with the obtained total Tm concentrations from the ICP-OES, it follows that the $BaCl_2$:$Tm^{2+/3+}$ sample contains about 0.3 mol % Tm^{2+} and 0.8 mol % Tm^{3+}, and the $BaCl_2$:Tm^{3+} sample contains around 1.5 mol % Tm^{3+}. A summary overview of the determined Tm^{2+} and Tm^{3+} concentrations in the investigated samples is provided in Table 1.

3.2. Relative energies of Tm^{2+} $4f^{12}5d^1$ and $4f^{13}$ excitation levels

With their structural properties established and the Tm^{2+}- and Tm^{3+}-doping concentrations estimated in the $BaCl_2$:Tm^{3+} and $BaCl_2$:$Tm^{2+/3+}$ samples, the relative energies between the Tm^{2+} $4f^{13}$-and $4f^{12}5d^1$-energy levels were examined using the $BaCl_2$:$Tm^{2+/3+}$ sample. Fig. 3 shows the Tm^{2+} emission pattern in orthorhombic $BaCl_2$ after exciting into the Tm^{2+} $(^3H_6, 5\ d^1)_{S\ =\ 1/2}$ $4f^{12}5d^1$-levels. At 20 K two $4f^{12}5d^1 \rightarrow 4f^{13}$ emissions are observed together with the $^2F_{5/2} \rightarrow {}^2F_{7/2}$ ($4f^{13} \rightarrow 4f^{13}$) emission. At room temperature only the latter emission remains. In our previous work on orthorhombic $BaCl_2$:Tm^{2+} [20] we classified the two $4f^{12}5d^1 \rightarrow 4f^{13}$ emissions as the $(^3H_6, 5\ d^1)_{S\ =\ 1/2} \rightarrow {}^2F_{7/2}$ Spin-Allowed (SA) transition and $(^3H_6, 5\ d^1)_{S\ =\ 3/2} \rightarrow {}^2F_{7/2}$ the Spin-Forbidden (SF) transition. For the $^2F_{5/2} \rightarrow {}^2F_{7/2}$ emission, excitation spectra were made at 20K (blue) and 300K (red) as shown in Fig. 4. In this figure, the lowest energy $4f^{12}5d^1$-levels are labelled in close analogy to the work of Grimm et al. as $(^3H_6, 5\ d^1)_{S\ =\ 1/2}$ and $(^3H_6, 5\ d^1)_{S\ =\ 3/2}$ [12]. As Tm^{2+} occupies the single asymmetric Ba^{2+} site with long distances in orthorhombic $BaCl_2$, the Tm^{2+} $4f^{12}5d^1$-levels undergo a rather small crystal field splitting.

Table 1
Overview of the estimated Tm^{2+} and Tm^{3+} concentrations in the samples via ICP-OES and Kubelka-Munk absorption.

Sample:	mol % TmI_2 [a]	mol % $TmCl_3$ [a]	mol % Tm [b]	Tm^{2+}/ Tm^{3+} ratio [c]	mol % Tm^{2+} [d]	mol % Tm^{3+} [d]
$BaCl_2$: $Tm^{2+/3+}$	1.0	–	1.1	3/8	0.3	0.8
$BaCl_2$: Tm^{3+}	–	1.5	1.5	0/1	0.0	1.5

[a] a) nominal doping b) ICP-OES c) K-M absorption spectra d) calculated from ICP-OES and K-M absorption spectra.

This results in a close packing of the $4f^{12}5d^1$-levels, which allows it to only distinguish and classify the lower energy $4f^{12}5d^1$-levels. These comprise of the $(^3H_6, 5\ d^1)_{S\ =\ 1/2}$ Low Spin (LS) levels located at around 570 nm (or 2.18 eV) and the $(^3H_6, 5\ d^1)_{S\ =\ 3/2}$ High Spin (HS) levels positioned close by 630 nm (or 1.97 eV) [12,20]. Upon including the Tm^{2+} $^2F_{7/2} \rightarrow {}^2F_{5/2}$ ($4f^{13} \rightarrow 4f^{13}$) absorption peak (magenta) from the K-M absorption spectrum (see Fig. 2), which is positioned at around 1140 nm (or 1.09 eV), the energy level scheme positioned at the right of Figs. 3 and 4 can be established. This scaled scheme shows the positioning of the Tm^{2+} $^2F_{5/2}$ $4f^{13}$-level and the $(^3H_6, 5\ d^1)_{S\ =\ 1/2}$ LS and $(^3H_6, 5\ d^1)_{S\ =\ 3/2}$ HS $4f^{12}5d^1$-levels as relative to the $^2F_{7/2}$ $4f^{13}$ ground state level.

3.3. Bandgap of $BaCl_2$ host lattice and Tm^{3+}-Cl^- charge transfer energy

For Tm^{2+} as doped in orthorhombic $BaCl_2$, the rather small $4f^{12}5d^1$ crystal field splitting results in the.

$(^3H_6, 5\ d^1)_{S\ =\ 1/2}$ LS and $(^3H_6, 5\ d^1)_{S\ =\ 3/2}$ HS levels to be located at quite high energy for a halide host lattice [12]. This raises the question whether these emitting levels might be positioned closely to the conduction band of the $BaCl_2$ host lattice. To verify this, the bandgap energy of the orthorhombic $BaCl_2$ host should be determined and the relative positioning of the Tm^{2+} levels with respect to the Conduction Band (CB) or Valence Band (VB) of the $BaCl_2$ host lattice needs to be established. In case of the latter, the Tm^{3+}-Cl^- Charge Transfer (CT) energy can be used, as it resembles the energy difference between the top of the VB and the Tm^{2+} $^2F_{7/2}$ $4f^{13}$ ground state [29]. Upon using this Tm^{3+}-Cl^- CT energy in combination with the relative energies between the Tm^{2+} $4f^{13}$-and $4f^{12}5d^1$-energy levels (from the previous subsection), together with the $BaCl_2$ bandgap energy; it becomes possible to deduce the relative positioning of the Tm^{2+} emitting $4f^{12}5d^1$-levels in relation to the CB of the $BaCl_2$ host lattice. For this purpose, the Tm^{3+}-Cl^- CT energy is thus an essential parameter which can be obtained with.

help of the $BaCl_2$:Tm^{3+} sample, as will be discussed subsequently.

Fig. 5 reveals several Tm^{3+} emissions after exciting the $BaCl_2$:Tm^{3+} sample at 350 nm, into the Tm^{3+} $^1D_2$ level. These emissions can be classified with help of the Dieke diagram [28] and previous Tm^{3+} VUV-NIR studies [30–32]; and comprise of: the $^1D_2 \rightarrow {}^3F_4$ emission at 440 nm, the $^1G_4 \rightarrow {}^3H_6$ emission at 465 nm, the $^3F_{2,3} \rightarrow {}^3H_6$ emission at 705 nm, the $^3H_4 \rightarrow {}^3H_6$ emission at 810 nm and the $^3H_5 \rightarrow {}^3H_6$ emission at 1230 nm. For most of these Tm^{3+} emissions, a low temperature excitation spectrum was recorded, extending from the VUV to the NIR. The resulting spectra are displayed in the top panel of Fig. 6, with a scaled energy level scheme presented alongside. In these spectra various narrow and weak excitation peaks can be distinguished between 260 and

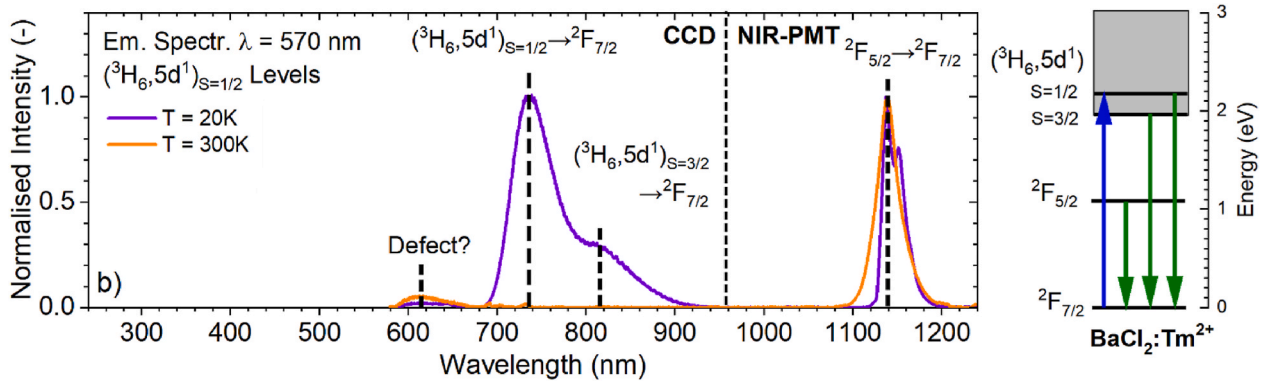

Fig. 3. Normalized VIS and NIR emission spectra of Tm^{2+} as doped in orthorhombic $BaCl_2$ at 20 and 300 K. Photoexcitation occurred at 570 nm into the Tm^{2+} $(^3H_6,5\ d^1)_{S\ =\ 1/2}$ levels. The emissions are classified in accordance to our recent work on $BaCl_2$:Tm^{2+} [20] with a scaled energy level scheme provided on the right. Three distinct Tm^{2+} emissions can be observed: the $(^3H_6,5\ d^1)_{S\ =\ 1/2} \rightarrow {}^2F_{7/2}$ Spin-Allowed (SA) emission at 720 nm, the $(^3H_6,5\ d^1)_{S\ =\ 3/2} \rightarrow {}^2F_{7/2}$ Spin-Forbidden (SF) emission at 815 nm and the spin and parity forbidden $^2F_{5/2} \rightarrow {}^2F_{7/2}$ emission at 1140 nm. A weak emission due to a defect or an artefact of the hygroscopic sample holder can be observed near 615 nm.

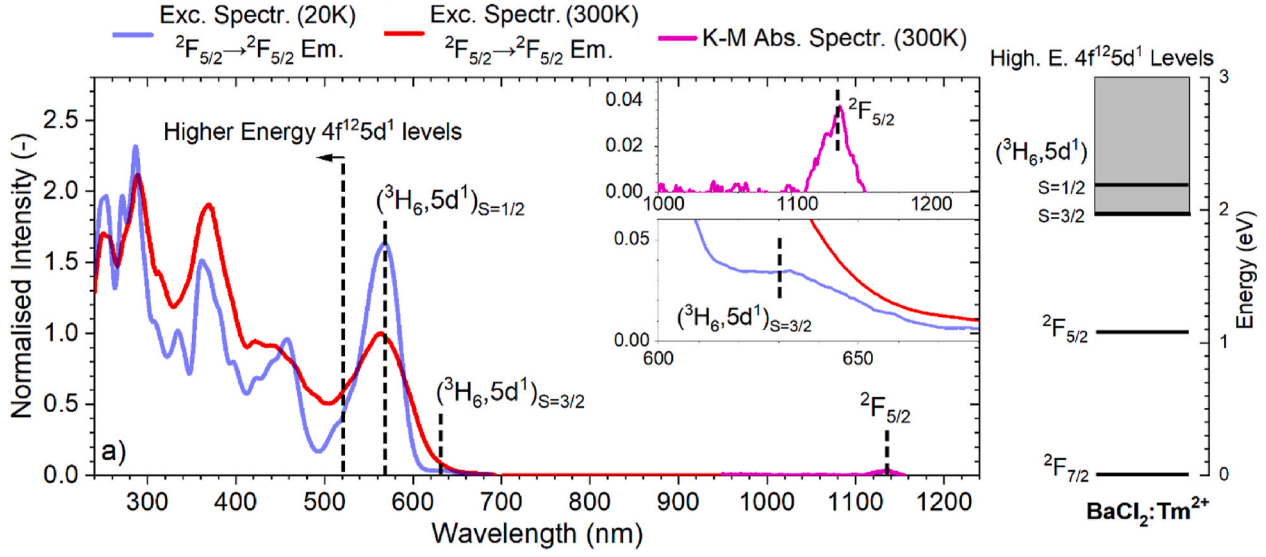

Fig. 4. The excitation spectrum as acquired on the Tm^{2+} $^2F_{5/2} \rightarrow {}^2F_{7/2}$ emission at 20K (blue) and 300K (red), showing the $(^3H_6,5\ d^1)_{S\ =\ 1/2}$ Low Spin (LS) and $(^3H_6,5\ d^1)_{S\ =\ 3/2}$ High Spin (HS) $4f^{12}5d^1$-levels of the $BaCl_2$:$Tm^{2+/3+}$ sample. In addition, a part of the K-M absorption spectrum with the Tm^{2+} $^2F_{5/2}$ $4f^{13}$-level is included (magenta). The spectra allow it to establish the Tm^{2+} energy level scheme positioned at the right, where the $(^3H_6,5\ d^1)_{S\ =\ 1/2}$ LS and $(^3H_6,5\ d^1)_{S\ =\ 3/2}$ HS $4f^{12}5d^1$-levels and the $^2F_{5/2}$ $4f^{13}$-level are positioned as relative to the $^2F_{7/2}$ $4f^{13}$ ground state level.

900 nm. Upon comparing with the Dieke diagram [28], the peaks can be related to specific Tm^{3+} $4f^{12} \rightarrow 4f^{12}$ transitions and are labelled as such in the spectra. In addition, a packed cluster of broad and intense peaks ranging from 180 to 245 nm can be observed. The Dieke diagram [28], the tabulated data from Carnall et al. [33] and the study by Wegh et al. [34] show that there are no Tm^{3+} $4f^{12} \rightarrow 4f^{12}$ transitions present within the wavelength range of 180–260 nm. Moreover, the lowest energy Tm^{3+} $4f^{12} \rightarrow {}^24f^{11}5d^1$ transition is to be expected at 7.51 eV or 165 nm and thus also falls outside of the energy range of the cluster [35]. We therefore expect that the packed cluster of broad and intense peaks may include: a peak related to the Tm^{3+}-Cl^- CT transition, a bound exciton creation peak that is associated with the bandgap of the $BaCl_2$ host and possibly peaks related to additional excitonic features.

3.3.1. *Gaussian deconvolution and analysis*

To come to an assignment and estimate for the energy of the Tm^{3+}-Cl^- CT transition and the $BaCl_2$ host lattice exciton creation peak, a first order approach was used in the form of an energy-scale Gaussian deconvolution on the packed cluster of peaks. Such a deconvolution was performed on each of the Tm^{3+} excitation spectra in Fig. 6, with the assumption of a constant quantum efficiency that is wavelength independent. Moreover, the excitation spectra were converted from wavelength scale to energy scale using the following relation: $\Phi_E = \Phi_\lambda \bullet \lambda^2 \bullet (hc)^{-1}$ [36]. For all four spectra, an accurate fit ($R^2 \geq 0.9996$) could be obtained using a four-peak-deconvolution. In case of a three-peak deconvolution no fitting convergence could be established, whereas for a five-peak-deconvolution the fits were highly inaccurate ($R^2 \approx 0.9889$) or yielded unrealistic results. For the four-peak-deconvolution, the results for the Tm^{3+} excitation spectra are displayed in the top panel in Fig. 7, with close-ups presented in sections 9.1-4 in the Supplementary Information (SI). Furthermore, Table 2 provides a detailed list of the retrieved Gaussian parameters. Upon mutually comparing the energy centres of the four peaks in every spectrum, up to five different peaks can be identified in total. These peaks are distinctively labelled (1) to (5) in Table 2 and coloured in Fig. 7. Of these five peaks, one peak has to match with the Tm^{3+}-Cl^- CT transition peak and another one can be coupled to that of $BaCl_2$ host lattice exciton creation. The remaining peaks will likely represent additional excitonic features.

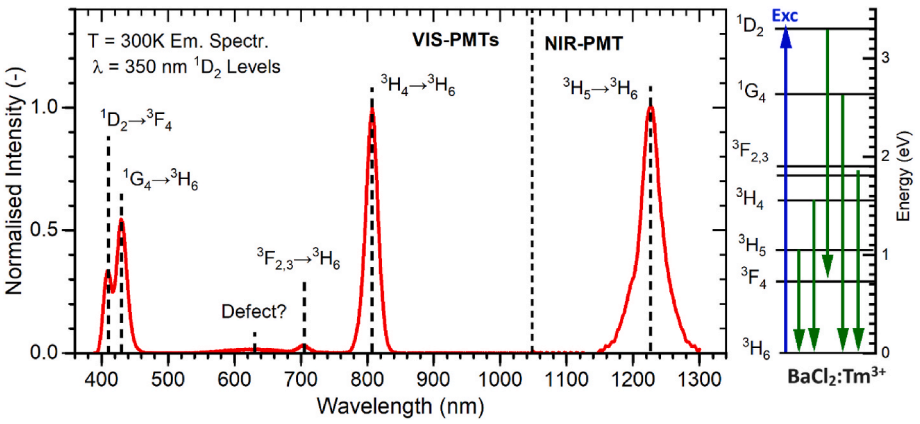

Fig. 5. Normalized VIS and NIR emission spectra at 300 K of Tm^{3+} as doped in orthorhombic $BaCl_2$. Photoexcitation occurred at 350 nm into the Tm^{3+} $^1D_2$ levels. Five distinct Tm^{3+} emissions can be observed, which are classified in accordance to the Dieke diagram [28]. For convenience, a scaled energy level scheme is provided on the right showing the excitation and emission by their transition. A weak emission due to a defect or an artefact of the hygroscopic sample holder can be observed near 615 nm.

In a similar way, an excitation spectrum was also made on the Tm^{2+} $^2F_{5/2} \rightarrow {}^2F_{7/2}$ emission, using the $BaCl_2:Tm^{2+}$ sample. The resulting spectrum is shown in purple in the lower panel of Fig. 6. Beside the Tm^{2+} $4f^{12}5d^1$ excitation bands present up to 640 nm, a packed cluster of broad and intense peaks situated from 180 to 220 nm can be observed that shares an analogy with the excitation spectra acquired on the Tm^{3+} emissions. As the Tm^{2+}-Cl^- CT transition is expected at a very high energy (i.e. at wavelengths lower than 180 nm) [29,37–40], this cluster of peaks is likely to contain the bound exciton creation peak related to the $BaCl_2$ host bandgap and additional excitonic features. A similar Gaussian deconvolution procedure was performed on the Tm^{2+} excitation spectrum, where a three-peak-deconvolution yielded an accurate fit (R^2 = 0.9989). The results of the deconvolution are displayed in the bottom panel of Fig. 7 and in section 7.5 of the SI. The Gaussian parameters retrieved from the deconvolution are listed in Table 3. Upon comparing the three peaks from the Tm^{2+} excitation spectrum, with the five peaks retrieved from the Tm^{3+} spectra, the energy centres are very similar. The three peaks from the Tm^{2+} excitation spectrum are therefore labelled (1), (2) and (3) in accordance to the Tm^{3+} excitation spectra, using the same colour scheme in Fig. 7.

Upon comparing, peaks (4) and (5) are only present in the Tm^{3+} spectra, not in the Tm^{2+} spectrum. Moreover, peak (5) is present in all Tm^{3+} spectra. It is thus very likely that peaks (4) and (5), respectively centred at an average energy of 5.5 ± 0.1 and 5.1 ± 0.1 eV, represent Tm^{3+} charge transfer transitions. For $BaCl_2:Tm^{3+}$ only a single charge transfer band is expected related to the Tm^{3+}-Cl^- transition, so the second charge transfer band may be related to the Tm^{3+}-O^{2-} CT transition due to the presence in minor amounts of O^{2-} on the Cl^- site for charge compensating Tm^{3+} replacing Ba^{2+}. An analogous situation has been reported for the CT transition of Rare-Earth (RE) ions doped in YF_3 or LaF_3 containing some traces of O^{2-}: in addition to the RE^{3+}-F^- charge transfer band also the RE^{3+}-O^{2-} band was observed [41]. For $BaCl_2:Tm^{3+}$ the low energy charge transfer transition at 5.1 ± 0.1 eV is ascribed to the CT of Tm^{3+}-Cl^-, while the high energy charge transfer transition at 5.5 ± 0.1 eV is attributed to the CT of Tm^{3+}-O^{2-} due to the electronegativity of O higher than that of Cl [42].

In addition, peak (1) is present in the Tm^{2+} spectrum and all of the Tm^{3+} spectra. Peaks (2) and (3) are also present in the Tm^{2+} spectrum, but are not observed in every Tm^{3+} spectrum. We therefore suspect that peak (1), centred at an average energy of 6.97 ± 0.1 eV, might represent the bound exciton creation peak of the $BaCl_2$ host lattice as confirmed by the observation of an exciton excitation peak at about 178 nm (6.97 eV) for a $BaCl_2$ single crystal [43]. From the exciton peak at 6.97 eV, the band gap energy $E_{VB\text{-}CB}$ of orthorhombic $BaCl_2$ can be calculated to be about 1.08 × 6.97 eV = 7.53 eV [44,45]. This value resembles very well with the band gap estimated from band structure calculations (7.5 eV) [46]. In addition, somewhat lower and higher values are reported: a bandgap energy of 7.0 eV was measured from X-ray absorption and emission spectra [47], while a higher band gap energy of approximately 8.5 eV was reported for absorption measurements in the 120–200 nm wavelength region [48]. Summarizing, the bandgap energy of orthorhombic $BaCl_2$ at room temperature is in the range 7.0–8.5 eV. Considering the reliability of the experimental values reported in the various publications, the agreement with band structure calculations and the value determined in this work; the most sound bandgap energy of orthorhombic $BaCl_2$ is 7.5 eV.

3.4. *Positioning of Tm^{2+} $4f^{12}5d^1$ and $4f^{13}$ levels versus $BaCl_2$ bandgap (VB/CB)*

Fig. 8 shows the Host-Referred Binding Energy (HRBE) scheme for orthorhombic $BaCl_2:Tm^{2+}$, constructed with the determined input parameters: the estimated $BaCl_2$ bandgap energy $E_{VB\text{-}CB}$ (green arrow), the Tm^{3+}-Cl^- charge transfer energy (red arrow) and the energies of the Tm^{2+} $4f^{13}5d^1$ excitation levels (black horizontal bars). The $^2F_{5/2}$ $4f^{13}$-level was found to be positioned at 1.09 ± 0.1 eV higher energy than the $^2F_{7/2}$ $4f^{13}$ ground state level; whereas for the $(^3H_6,5\ d^1)_{S\ =\ 3/2}$ HS and $(^3H_6,5\ d^1)_{S\ =\ 1/2}$ LS $4f^{12}5d^1$-levels, the relative energy difference with the $^2F_{7/2}$ ground state level respectively amounted to 1.97 ± 0.1 and 2.18 ± 0.1 eV. Note that the energy of the top of the valence band is placed at 0 eV. As illustrated by the figure, the Tm^{3+}-Cl^- CT energy corresponds with the energy difference between the top of the VB of the $BaCl_2$ host and the energy of the Tm^{2+} $^2F_{7/2}$ ground state [36,43,44]. Hence, it is crucial in determining the position of the Tm^{2+} $4f^{12}5d^1$ and $4f^{13}$ excitation levels versus the CB of the $BaCl_2$ host lattice.

According to this analysis, the Tm^{2+} $(^3H_6,5\ d^1)_{S\ =\ 3/2}$ HS and $(^3H_6,5\ d^1)_{S\ =\ 1/2}$ LS $4f^{12}5d^1$ levels are respectively positioned 0.5 and 0.3 eV below the conduction band of $BaCl_2$, and consequently one would clearly expect to observe a low temperature luminescence signal from those levels. This is indeed supported by the 20K emission spectra presented in Fig. 3 and our previous study on orthorhombic $BaCl_2:Tm^{2+}$ [20].

As independent evidence, the assignment of the 5.5 eV peak to the Tm^{3+}-O^{2-} CT transition is supported by the constructed energy level scheme shown in Fig. S6 in the SI. It shows that if the 5.5 eV peak was attributed to the Tm^{3+}-Cl^- CT transition, the lowest energy Tm^{2+} $4f^{12}5d^1$ levels are positioned either inside the conduction band of $BaCl_2$ or just slightly below it. With the $(^3H_6,5\ d^1)_{S\ =\ 1/2}$ LS levels located inside the conduction band, there would be a rather small chance of measuring low temperature $(^3H_6,5\ d^1)_{S\ =\ 1/2} \rightarrow {}^2F_{7/2}$ luminescence [49]. Yet, this

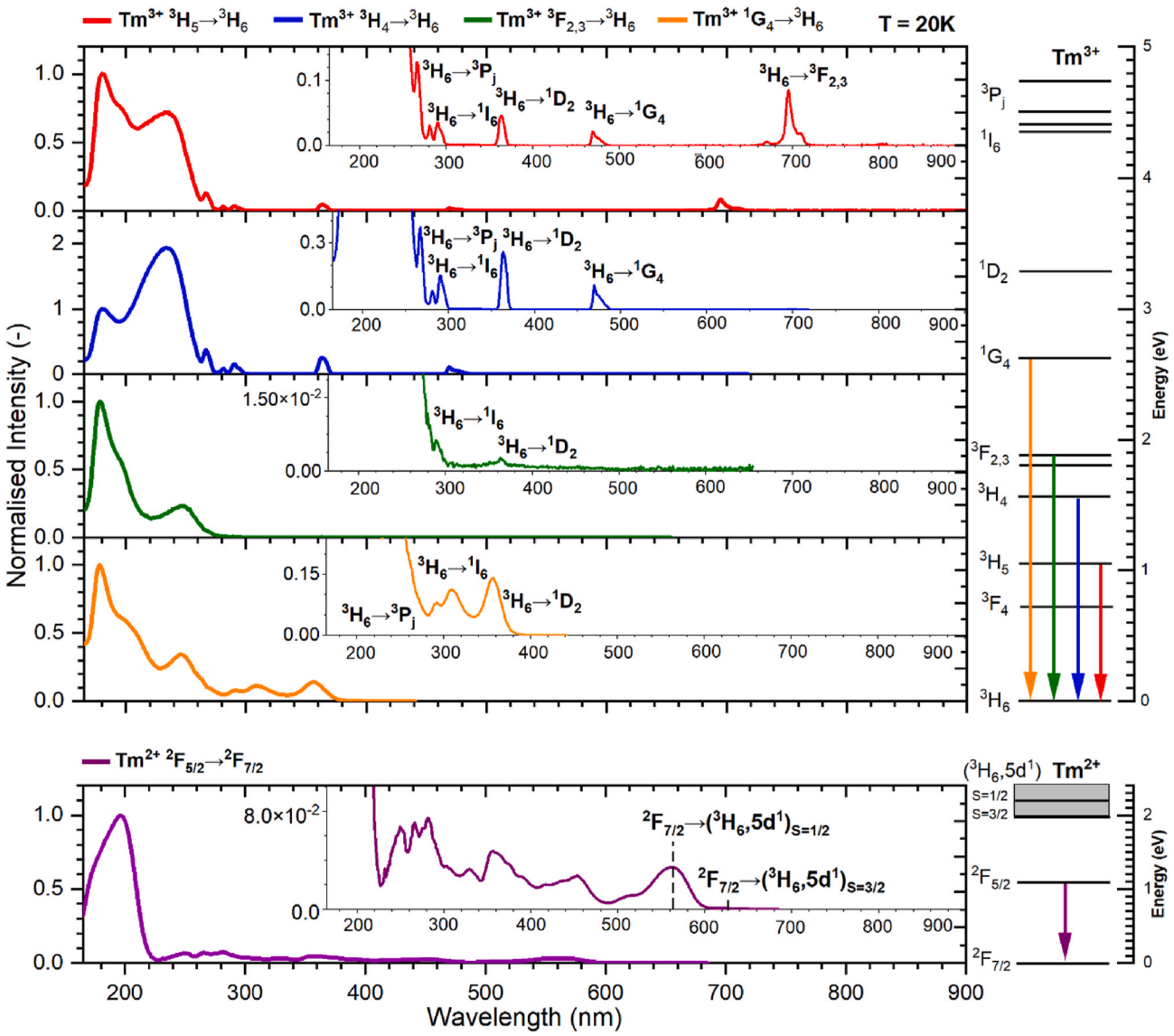

Fig. 6. VUV-NIR Excitation spectra as acquired on various Tm^{3+} emissions shown by the orthorhombic $BaCl_2$:Tm^{3+} sample. The colour of the spectra matches the colour of the arrow corresponding with the transition in the scaled energy level diagram to the right. The narrow and weak Tm^{3+} excitation bands are labelled in accordance to their transition. The packed cluster of peaks between 180 and 245 nm is likely to contain the $BaCl_2$ host lattice exciton creation peak and Tm^{3+}-Cl^- charge transfer band. The lower panel shows the VUV-NIR excitation spectrum obtained for the Tm^{2+} $^2F_{5/2} \rightarrow {}^2F_{7/2}$ emission of the orthorhombic $BaCl_2$:$Tm^{2+/3+}$ sample. This spectrum also displays a series of closely spaced peaks between 180 and 245 nm, among which the $BaCl_2$ host lattice exciton creation peak, and various Tm^{2+} $4f^{12}5d^1$ levels. All spectra were measured at 20 K.

luminescence was previously captured by us in the temperature range of 20–120 K [20]. Moreover, it was even found to be more intense than the $(^3H_6,5\ d^1)_{S\ =\ 3/2} \rightarrow {}^2F_{7/2}$ luminescence, that originates from the $(^3H_6,5\ d^1)_{S\ =\ 3/2}$ HS $4f^{12}5d^1$-levels, supposedly located 0.1 eV below the conduction band (Fig. S6 in SI). Also for the $4f^{12}5d^1$-levels close to or inside the conduction band, anomalous emission may be expected, characterized by a Stokes shift larger than 0.6 eV [50]. Tables S6 and S7 in the SI show that there is no significant shift in the energies of the emissions and excitation levels, as a function of the sample temperature. Moreover, for orthorhombic $BaCl_2$:Tm^{2+}, the Stokes shifts of the $(^3H_6,5\ d^1)_{S\ =\ 1/2} \rightarrow {}^2F_{7/2}$ SA and $(^3H_6,5\ d^1)_{S\ =\ 3/2} \rightarrow {}^2F_{7/2}$ SF emissions respectively amount to about 0.50 and 0.45 eV, which is below the aforementioned threshold value.

3.5. *Implications of position of $BaCl_2$ CB on the thermal quenching of Tm^{2+} luminescence*

As deduced in the previous subsection, the Tm^{2+} $(^3H_6)_{S\ =\ 1/2}$ LS $4f^{12}5d^1$-levels are likely to be located very close to the bottom of the $BaCl_2$ conduction band. Electrons excited in these levels can undergo thermal ionization with rising temperature from the Tm^{2+} luminescence centre towards the $BaCl_2$ conduction band and form an Tm^{3+} impurity bound or unbound (free) exciton state. For impurity bound exciton states, the electron remains localised on Tm^{3+} and undergoes either a non-radiative or radiative recombination. The latter is often referred to as impurity bound exciton emission or anomalous emission, which is not observed for orthorhombic $BaCl_2$:Tm^{2+} due to the Stokes shift being smaller than expected [50]. In case of unbound (free) exciton states, the electrons become delocalised from the Tm^{3+} impurity ions and constitute a thermally induced photocurrent that eventually recombines non-radiatively with a hole in the valence band [49,51,52].

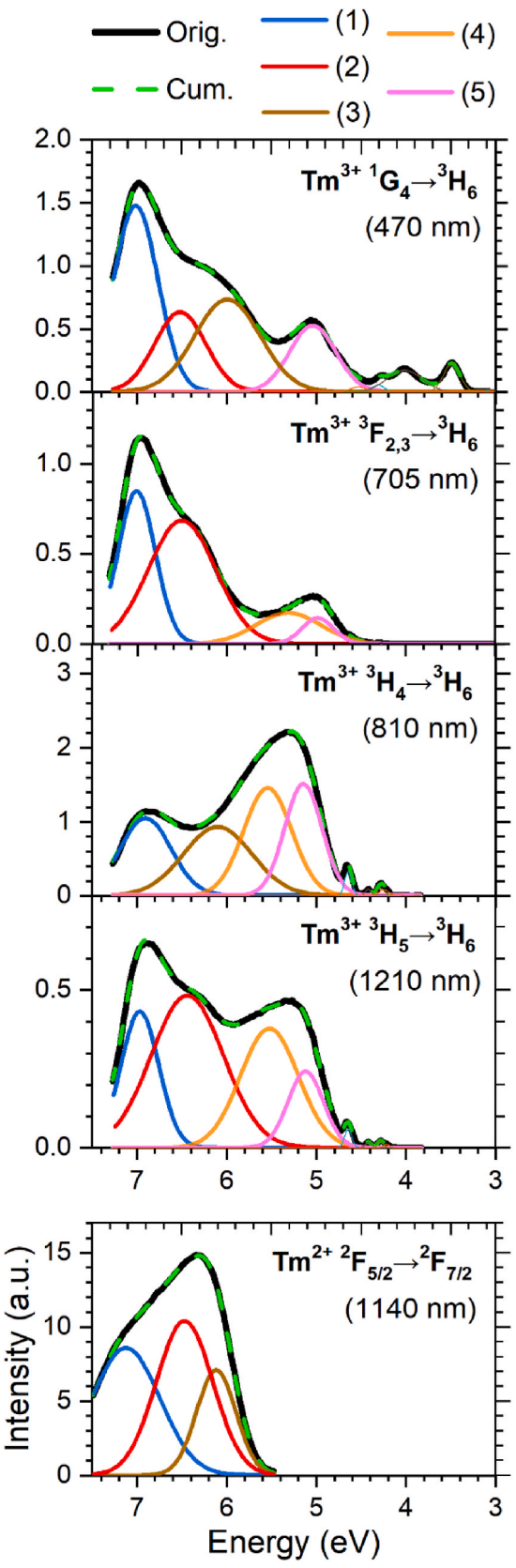

Fig. 7. Gaussian, energy scale, deconvolution of the excitation spectra of Fig. 6, focussing on the packed clusters of broad and intense peaks portrayed between 180 and 245 nm. The clusters related to the Tm^{3+} excitation spectra could each be accurately deconvoluted into four peaks, while for the Tm^{2+} excitation spectrum three identical peaks could be separated. About the whole, five peaks could be distinguished.

Since the $(^3H_6,5\ d^1)_{S\ =\ 1/2}$ LS levels of $BaCl_2$:Tm^{2+} are so close to the $BaCl_2$ conduction band, thermal ionization processes are likely to be triggered already at relatively low temperatures. In our previous work on $BaCl_2$:Tm^{2+} [20], where we excited into the $(^3H_6,5\ d^1)_{S\ =\ 1/2}$ LS levels, we noticed that the intensity of the $^2F_{5/2} \rightarrow {}^2F_{7/2}$ emission suddenly dropped by around 17 % as the temperature increased from 90 to 350 K. We attributed this observation to the presence of a $(^3H_6,5\ d^1)_{S\ =\ 1/2} \rightarrow {}^2F_{7/2}$ and $(^3H_6,5\ d^1)_{S\ =\ 3/2} \rightarrow {}^2F_{7/2}$ ground state quenching route via interband crossing. However, after considering the potential influence of the conduction band of the $BaCl_2$ host lattice on the thermal quenching, the sudden decrease in $^2F_{5/2} \rightarrow {}^2F_{7/2}$ luminescence might also involve a contribution impending from non-radiative thermal ionization effects. This could also explain why the measured quantum yield of the $^2F_{5/2} \rightarrow {}^2F_{7/2}$ emission at room temperature is non-unity.

In this context, the recent work of Radzhabov et al. [5] on Tm^{2+}-doped BaF_2, SrF_2 and CaF_2 shows independent support for our point of view. It shows a clear correlation between the quenching temperature of the $^2F_{5/2} \rightarrow {}^2F_{7/2}$ ($4f^{13} \rightarrow 4f^{13}$) emission and the energy difference between the Tm^{2+} excitation level and the bottom of the host lattice conduction band. These energy differences were found to resemble 0.57, 0.87, 0.96 eV for BaF_2, SrF_2 and CaF_2, respectively, while the respective quenching temperatures amounted to 250, 300, 350 K. However, in that study photoexcitation occurred in the $^2F_{5/2}$ $4f^{12}$-level and not in the higher energy $(^3H_6,5\ d^1)_{S\ =\ 1/2}$ LS $4f^{12}5d^1$-levels as exercised by us. Nevertheless, it confirms that quenching effects related to the $BaCl_2$ host-lattice conduction band are quite probable to take place at low temperature.

4. Summary and conclusions

In this work, we have examined the positioning of the Tm^{2+} $4f^{12}5d^1$ and $4f^{13}$ energy levels as relative to the conduction band of the orthorhombic $BaCl_2$ host lattice. At first, a room temperature excitation spectrum was made on the Tm^{2+} $4f^{13} \rightarrow 4f^{13}$ emission, using the $BaCl_2$:$Tm^{2+/3+}$ sample, to reveal the energies of the Tm^{2+} $4f^{12}5d^1$-and $4f^{13}$-levels as relative to the Tm^{2+} $4f^{13}$ ground state. For the $(^3H_6,5\ d^1)_{S\ =\ 1/2}$ LS and $(^3H_6,5\ d^1)_{S\ =\ 3/2}$ HS lowest energy $4f^{12}5d^1$-levels, the relative energy with the $^2F_{7/2}$ $4f^{13}$ ground state was respectively found to resemble 2.18 eV and 1.98 eV. For the $^2F_{5/2}$ $4f^{13}$-level, this relative energy was established at 1.09 eV. Using the $BaCl_2$:Tm^{3+} sample, excitation spectra into the vacuum ultra violet were made onto various Tm^{3+} $4f^{12} \rightarrow 4f^{12}$ emissions. These spectra displayed a packed clusters of broad and intense peaks, portrayed between 180 and 245 nm, onto which an energy scale Gaussian deconvolution was performed. The clusters were found to each consist of four different peaks, while overall five distinct peaks could be recognised. Using the $BaCl_2$:$Tm^{2+/3+}$ sample, an analogous analysis was performed on the Tm^{2+} excitation spectra of the $4f^{13} \rightarrow 4f^{13}$ emission, yielding three different peaks at energies similar to those stemming from the Tm^{3+} excitation spectra. Subsequently, the different peaks were analyzed and compared with literature data. A peak present in both the Tm^{3+} and Tm^{2+} excitation spectra, centred at 6.97 ± 0.1 eV, could be attributed to bound exciton creation from which the $BaCl_2$ bandgap energy was calculated to represent 7.5 ± 0.1 eV. In addition, a peak centred at 5.1 ± 0.1 eV, which is only present in the Tm^{3+} excitation spectra, was linked to the Tm^{3+}-Cl^- charge transfer transition. Upon using the $BaCl_2$ bandgap energy, the Tm^{3+}-Cl^- charge transfer transition and the energies of the Tm^{2+} $4f^{12}5d^1$-and $4f^{13}$-levels as relative to the Tm^{2+} $4f^{13}$ ground state, a host referred binding energy scheme was constructed. From this scheme, the Tm^{2+} $(^3H_6,5\ d^1)_{S\ =\ 1/2}$ LS and $(^3H_6,5\ d^1)_{S\ =\ 3/2}$ HS $4f^{12}5d^1$-levels were found to be respectively positioned about 0.3 and 0.5 eV below the $BaCl_2$ conduction band. This is consistent with the observation of the Tm^{2+} $(^3H_6,5\ d^1)_{S\ =\ 1/2} \rightarrow {}^2F_{7/2}$ SA and $(^3H_6,5\ d^1)_{S\ =\ 3/2} \rightarrow {}^2F_{7/2}$ SF emissions at temperatures between 20 and 120 K. As the Tm^{2+} $(^3H_6,5\ d^1)_{S\ =\ 1/2}$ LS and $(^3H_6,5\ d^1)_{S\ =\ 3/2}$ HS $4f^{12}5d^1$-levels are closely positioned to the $BaCl_2$ conduction band, photoexcitation into these levels will introduce thermal ionization

Table 2
Gaussian parameters describing the deconvoluted peaks present in the Tm^{3+} excitation spectra.

	$^1G_4 \rightarrow {}^3H_6$ (470 nm)			$^3F_{2,3} \rightarrow {}^3H_6$ (705 nm)			$^3H_4 \rightarrow {}^3H_6$ (810 nm)			$^3H_5 \rightarrow {}^3H_6$ (1230 nm)		
	C (eV)	Rl. H (−)	F (eV)	C (eV)	Rl. H (−)	F (eV)	C (eV)	Rl. H (−)	F (eV)	C (eV)	Rl. H (−)	F (eV)
(1)	7.01 ± 0.1	1.0	0.58	7.01 ± 0.1	1.0	0.49	6.90 ± 0.1	0.69	0.64	6.97 ± 0.1	0.89	0.50
(2)	6.52 ± 0.1	0.43	0.67	6.50 ± 0.1	0.81	0.89	–	–	–	6.44 ± 0.1	1.0	0.95
(3)	5.99 ± 0.1	0.50	0.86	–	–	–	6.10 ± 0.1	0.62	1.05	–	–	–
(4)	–	–	–	5.31 ± 0.1	0.20	0.86	5.54 ± 0.1	0.96	0.72	5.53 ± 0.1	0.78	0.76
(5)	5.04 ± 0.1	0.36	0.61	4.98 ± 0.1	0.17	0.41	5.15 ± 0.1	1.0	0.46	5.12 ± 0.1	0.50	0.46

Note that: C = Centre of peak, Rl. H = Relative peak height, F = FHWM of peak.

Table 3
Similar as Table 2 only for the Tm^{2+} excitation spectrum.

	$^2F_{5/2} \rightarrow {}^2F_{7/2}$ (1140 nm)		
	C (eV)	Rl. H (−)	F (eV)
(1)	7.12 ± 0.1	0.83	0.89
(2)	6.47 ± 0.1	1.0	0.74
(3)	6.12 ± 0.1	0.68	0.52

Note that: C = Centre of peak, Rl. H = Relative peak height, F = FHWM of peak.

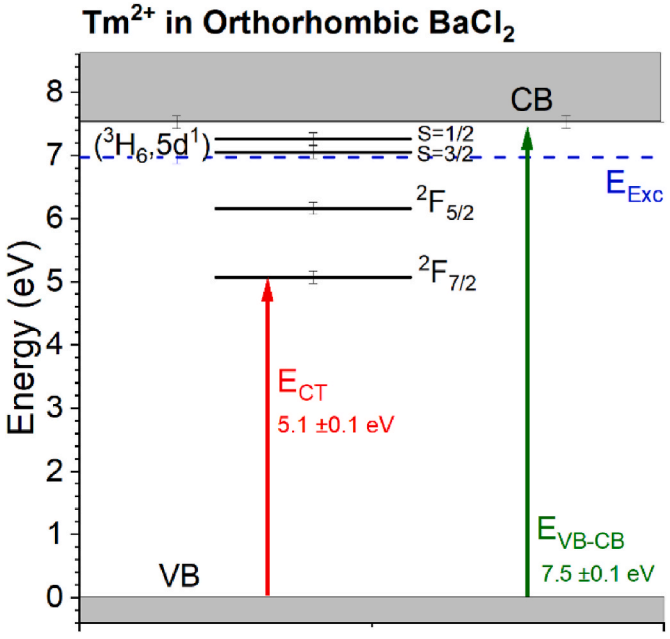

Fig. 8. Host-Referred Binding Energy (HRBE) scheme of orthorhombic $BaCl_2$: Tm^{2+} as based on: the bound-exciton energy E_{Exc} (dashed blue line), the estimated bandgap energy $E_{VB\text{-}CB}$ (green upward arrow) and the Tm^{3+}-Cl^- CT energy E_{CT} (red upward arrow). The Tm^{2+} $^2F_{7/2}$ and $^2F_{5/2}$ $4f^{13}$-levels and the $(^3H_6)_{S\ =\ 1/2}$ LS and $(^3H_6)_{S\ =\ 3/2}$ HS $4f^{12}5d^1$-levels are added in black. The bottom of the Conduction Band (CB) and the top of the Valence Band (VB) are represented by the upper and lower grey zones. Errors were estimated at 0.1 eV.

effects that are likely to compete with the $4f^{12}5d^1 \rightarrow 4f^{13}$ quenching routes described in our previous work [20]. Such effects will result in a temperature-dependent decrease of the $^2F_{5/2} \rightarrow {}^2F_{7/2}$ ($4f^{13} \rightarrow 4f^{13}$) luminescence and pose a limitation on its room temperature quantum yield.

Supporting information statement

This section contains: 9.1 Deconvolution of Tm^{3+} $^1G_4 \rightarrow {}^3H_6$ (470 nm) emission, 9.2 Deconvolution of Tm^{3+} $^3F_{2,3} \rightarrow {}^3H_6$ (705 nm) emission, 9.3 Deconvolution of Tm^{3+} $^3H_4 \rightarrow {}^3H_6$ (810 nm) emission, 9.4 Deconvolution of Tm^{3+} $^3H_5 \rightarrow {}^3H_6$ (1230 nm) emission, 9.5 Deconvolution of Tm^{2+} $^2F_{5/2} \rightarrow {}^2F_{7/2}$ (1140 nm) emission, 9.6 Host-Referred Binding Energy Scheme for $E_{CT} = 5.5 \pm 0.1$ eV and 9.7 Emission and excitation energies as a function of temperature.

CRediT authorship contribution statement

M.P. Plokker: Writing – review & editing, Writing – original draft, Visualization, Supervision, Software, Resources, Project administration, Methodology, Investigation, Formal analysis, Data curation, Conceptualization. **H.T. Hintzen:** Writing – review & editing, Writing – original draft, Visualization, Validation, Supervision, Resources, Project administration, Methodology, Funding acquisition, Conceptualization.

Declaration of competing interest

The authors declare the following financial interests/personal relationships which may be considered as potential competing interests: Maarten Plokker reports article publishing charges was provided by TU Delft. Dr. H.T. Hintzen reports a relationship with Delft University of Technology that includes: employment. If there are other authors, they declare that they have no known competing financial interests or personal relationships that could have appeared to influence the work reported in this paper.

Acknowledgement

This research was financially supported by the Department of Radiation Science & Technology at Delft University of Technology (TU Delft). The authors would like to thank ing. J.T.M. de Haas (TU Delft) for experimental support with the VUV-VIS luminescence measurements and ing. B.E. Terpstra (TU Delft) for overall assistance with ICP-OES measurements. Prof. P. Dorenbos is thank for valuable discussions about his models.

Appendix A. Supplementary data

Supplementary data to this article can be found online at https://doi.org/10.1016/j.omx.2024.100389.

Data availability

Data will be made available on request.

References

[1] Z.J. Kiss, Energy levels of divalent thulium in CaF_2, Phys. Rev. 127 (3) (1962) 718–724.
[2] D.S. McClure, Z. Kiss, Survey of the spectra of the divalent rare-earth ions in cubic crystals, J. Chem. Phys. 39 (12) (1963) 3251–3257.
[3] R.C. Duncan Jr., Z.J. Kiss, Continuously operating CaF_2:Tm^{2+} optical Maser, Appl. Phys. 3 (2) (1963) 23–24.
[4] Z.J. Kiss, R.J. Pressley, Crystalline solid lasers, Appl. Opt. 5 (10) (1966) 1474–1486.
[5] E. Radzhabov, R. Shendrik, V. Pankratov, Emission of Tm^{2+} in alkaline-earth fluoride crystals, J. Lumin. 252 (2022) 119271.

[6] O.S. Wenger, C. Wickleder, K.W. Krämer, H.U. Güdel, Upconversion in a divalent rare earth ion: optical absorption and luminescence spectroscopy of Tm^{2+} doped $SrCl_2$, J. Lumin. 94–95 (2001) 101–105.

[7] J. Grimm, E. Beurer, H.U. Güdel, Crystal absorption spectra in the region of 4f-4f and 4f-5d excitations in Tm^{2+}-doped $CsCaCl_3$, $CsCaBr_3$, and $CsCaI_3$, Inorg. Chem. 45 (2006) 10905–10908.

[8] J. Grimm, H.U. Güdel, Five different types of spontaneous emission simultaneously observed in Tm^{2+} doped $CsCaBr_3$, Chem. Phys. Lett. 404 (2005) 40–43.

[9] E. Beurer, J. Grimm, P. Gerner, H.U. Güdel, New type of near-infrared to visible photon upconversion in Tm^{2+}-doped $CsCaI_3$, J. Am. Chem. Soc. 128 (2006) 3110–3111.

[10] E. Beurer, J. Grimm, P. Gerner, H.U. Güdel, Absorption, light emission, and upconversion properties of Tm^{2+}-doped $CsCaI_3$ and $RbCaI_3$, Inorg. Chem. 45 (2006) 9901–9906.

[11] J. Grimm, J.F. Suyver, E. Beurer, G. Carver, H.U. Güdel, Light-emission and excited-state dynamics in Tm^{2+} doped $CsCaCl_3$, $CsCaBr_3$, and $CsCaI_3$, J. Phys. Chem. B 110 (2006) 2093–2101.

[12] J. Grimm, O.S. Wenger, K.W. Krämer, H.U. Güdel, 4f–4f and 4f–5d excited states and luminescence properties of Tm^{2+}-doped CaF_2, $CaCl_2$, $SrCl_2$ and $BaCl_2$, J. Lumin. 126 (2007) 590–596.

[13] J. Grimm, E. Beurer, P. Gerner, H.U. Güdel, Upconversion between 4f–5d excited states in Tm^{2+}-doped $CsCaCl_3$, $CsCaBr_3$, and $CsCaI_3$, Eur. J. Chem. 13 (2007) 1152–1157.

[14] O.M. ten Kate, K.W. Krämer, E. Van der Kolk, Efficient luminescent solar concentrators based on self-absorption free Tm^{2+} doped halides, Sol. Energy Mater. Sol. Cells 140 (2015) 115–120.

[15] M.P. Plokker, E. van der Kolk, Temperature dependent relaxation dynamics of luminescent NaX:Tm^{2+} (X=Cl, Br, I), J. Lumin. 216 (2019) 116694.

[16] M.P. Plokker, W. Hoogsteen, R.D. Abellon, K.W. Krämer, E. van der Kolk, Concentration and temperature dependent luminescence properties of the SrI2-TmI2 system, J. Lumin. 225 (2020) 117327.

[17] M.P. Plokker, I.C. van der Knijff, A.V. de Wit, B. Voet, T. Woudstra, V. Khanin, P. Dorenbos, E. van der Kolk, Experimental and numerical analysis of Tm^{2+} excited-states dynamics and luminescence in CaX_2 (X = Cl, Br, I), J. Phys. Condens. Matter 33 (25) (2021) 255701.

[18] M.P. Plokker, D.A. Biner, N. Dusoswa, P. Dorenbos, K.W. Krämer, E. van der Kolk, Photoluminescence and excited states dynamics of Tm^{2+}-doped $CsCa(Cl/Br)_3$ and $CsCa(Br/I)_3$ perovskites, J. Phys. Mater. 4 (4) (2021) 045004.

[19] C. Wickleder, Spectroscopic properties of $SrZnCl_4$:M^{2+} and $BaZnCl_4$:M^{2+} (M = Eu, Sm, Tm), J. Alloys Compd. 300–301 (2000) 193–198.

[20] M.P. Plokker, S. Vlaar, A.H.J. Bakx, E. van der Kolk, P. Dorenbos, H.T. Hintzen, Evaluating the Tm^{2+} $4f^{12}5d^1 \rightarrow 4f^{13}$ and $4f^{13} \rightarrow 4f^{13}$ luminescence and quenching dynamics in orthorhombic $BaCl_2$, J. Phys. Chem. 127 (38) (2023) 19017–19026.

[21] C.W. Struck, W.H. Fonger, Understanding Luminescence Spectra and Efficiency Using Wp and Related Functions, Inorganic Chemistry Concepts 13, Springer Verlag, 1991, 3-540-52766-4.

[22] M. Grinberg, T. Lesniewski, Non-radiative processes and luminescence quenching in Mn^{4+} doped phosphors, J. Lumin. 214 (2019) 116574.

[23] E.J. Iglesias, F. Mitschker, M. Fiebrandt, N. Bibinov, P. Awakowicz, In situ measurement of VUV/UV radiation from low-pressure microwave-produced plasma in Ar/O_2 gas mixtures, Meas. Sci. Technol. 28 (2017) 8.

[24] B. Moine, G. Bizarri, B. Varrel, J.Y. Rivoire, VUV-extended measurements of quantum efficiency of sodium salicylate and of some NBS standard phosphors, Opt. Matter. 29 (2007) 1148–1152.

[25] E. Rogers, P. Dorenbos, J.T.M. de Haas, E. van der Kolk, Experimental study of the $4f^n \rightarrow 4f^n$ and $4f^n \rightarrow 4f^{n-1}$ $5d^1$ transitions of the lanthanide diiodides LnI_2 (Ln = Nd, Sm, Eu, Dy, Tm, Yb), J. Phys. Condens. Matter 24 (2012) 27.

[26] L.H. Brixner, A. Ferretti, Eu^{2+} fluorescence in $BaCl_2$, J. Solid State Chem. 18 (1976) 111–116.

[27] R.D. Shannon, Revised effective ionic radii and systematic studies of interatomic distances in halides and chalcogenides, Acta Crystallogr. A32 (1976) 751–767.

[28] G.H. Dieke, H.M. Crosswhite, The spectra of the doubly and triply ionized rare earths, Appl. Opt. 2 (7) (1963) 675–686.

[29] P. Dorenbos, Systematic behaviour in trivalent lanthanide charge transfer energies, J. Phys. Condens. Matter 15 (49) (2003) 8417–8434.

[30] P. Villanueva, Delgado, K.W. Krämer, R. Valiente, M. de Jong, A. Meijerink, Modeling blue to UV upconversion in β-$NaYF_4$:Tm^{3+}, Phys. Chem. Chem. Phys. 18 (39) (2016) 27396–27404.

[31] B. Moine, L. Beauzamy, R.S. Meltzer, Thulium doped phosphors under VUV excitation, Mater. Res. Soc. Symp. Proc. 1111 (2008) 804.

[32] G.V. Lokeswara Reddy, L. Rama Moorthy, P. Perumal, C. Jamalaiah Bungala, Optical characterization of $YAl_3(BO_3)_4$:Dy^{3+}–Tm^{3+} phosphors under near UV excitation, Opt. Mater. 35 (12) (2013) 2138–2145.

[33] W.T. Carnall, G.L. Goodman, K. Rajnak, R.S. Rana, A systematic analysis of the spectra of the lanthanide doped into single crystal LaF_3, J. Mater. Chem. 90 (7) (1989) 3443.

[34] R.T. Wegh, A. Meijerink, R.J. Lamminmäki, J. Hölsä, Extending Dieke's diagram, J. Lumin. 87–89 (2000) 1002–1004.

[35] P. Dorenbos, The 5d level positions of the trivalent lanthanides in inorganic compounds, J. Lumin. 91 (2000) 155–176.

[36] G. Blasse, B.C. Grabmeier, Luminescent Materials - Appendix 4 – Equation, A4.1, Springer Verlag, 1994. ISBN-13: 978-3-540-58019-5.

[37] P. Dorenbos, An estimator for the Coulomb repulsion parameter U to generate vacuum referred binding energy schemes for lanthanides in compounds, J. Lumin. 267 (2024) 120358.

[38] P. Dorenbos, A. Josef, J.T.M. de Haas, K.W. Krämer, Vacuum referred binding energies of the lanthanides in chloride, bromide, and iodide compounds, J. Lumin. 208 (2019) 463–467.

[39] P. Dorenbos, Thermal quenching of lanthanide luminescence via charge transfer states in inorganic materials, J. Mater. Chem. C 11 (2023) 8129–8145.

[40] P. Dorenbos, Improved parameters for the lanthanide $4f^q$ and $4f^{q-1}5d$ curves in HRBE and VRBE schemes that takes the nephelauxetic effect into account, J. Lumin. 222 (2020) 117164.

[41] I. Gérard, J.C. Krupa, E. Simoni, P. Martin, Investigation of charge transfer $O^{2-} \rightarrow Ln^{3+}$ and $F^- \rightarrow Ln^{3+}$ in LaF_3:(Ln^{3+},O^{2-}) and YF_3:(Ln^{3+},O^{2-}) systems, J. Alloys Compd. 207/208 (3027) (1994) 120–127.

[42] C. Tantardini, A.R. Oganov, Thermochemical electronegativities of the elements, Nat. Commun. 12 (2021). Art. Nr. 2087.

[43] K. Onodera, M. Koshimizu, K. Asai, Luminescent properties of BaCl2 under VUV excitation, Radiat. Phys. Chem. 78 (2009) 1031–1033.

[44] P. Dorenbos, Charge transfer bands in optical materials and related defect level location, Opt. Mater. 69 (2017) 8–22.

[45] P. Dorenbos, The Eu3+ charge transfer energy and the relation with the band gap of compounds, J. Lumin. 111 (1) (2005) 89–104.

[46] A. Aguado, A. Ayuela, J.M. Lopez, J.A. Alonso, Calculation of the band gap energy and study of cross luminescence in alkaline-earth dihalide crystals, J. Phys. Soc. Jpn. 68 (8) (1999) 2829–2835.

[47] C. Sugiura, Chlorine-K X-ray spectra and electronic band structure of $MgCl_2$, $SrCl_2$, and $BaCl_2$, Phys. Rev. B 9 (6) (1974) 2679–2683.

[48] E. Nicklaus, Optical properties of some alkaline earth halides, Phys. Stat. Sol. 53 (1979) 217–224.

[49] G. Blasse, B.C. Grabmeier, Luminescent Materials, Springer Verlag, 1994. ISBN-13: 978-3-540-58019-5.

[50] P. Dorenbos, Anomalous luminescence of Eu2+ and Yb2+ in inorganic compounds, J. Phys.: Condens. Matter 15 (2003) 2645–2665.

[51] W.M. Yen, S. Shionoya, H. Yamamoto, Phosphor Handbook, second ed., vol. 2, CRC Press Taylor & Francis Group, 2007. ISBN 0-8493-3564-7.

[52] E. van der Kolk, J.T.M. de Haas, A.J.J. Bos, C.W.E. van Eijk, P. Dorenbos, Luminescence quenching by photoionization and electron transport in a LaAlO3:Ce3+ crystal, Int. J. Appl. Phys. 101 (2007) 083703.